Magic Angle–Enhanced MRI of Fibrous Microstructures in Sclera and Cornea With and Without Intraocular Pressure Loading

Leon C. Ho,[1-3] Ian A. Sigal,[2,4-6] Ning-Jiun Jan,[2,4] Alexander Squires,[7] Zion Tse,[7] Ed X. Wu,[3] Seong-Gi Kim,[1,4,5,8-10] Joel S. Schuman,[2,4-6,11] and Kevin C. Chan[1,2,4-6,8]

[1]NeuroImaging Laboratory, University of Pittsburgh, Pittsburgh, Pennsylvania, United States
[2]UPMC Eye Center, Ophthalmology and Visual Science Research Center, Department of Ophthalmology, School of Medicine, University of Pittsburgh, Pittsburgh, Pennsylvania, United States
[3]Department of Electrical and Electronic Engineering, The University of Hong Kong, Pokfulam, Hong Kong, China
[4]Department of Bioengineering, Swanson School of Engineering, University of Pittsburgh, Pittsburgh, Pennsylvania, United States
[5]McGowan Institute for Regenerative Medicine, University of Pittsburgh, Pittsburgh, Pennsylvania, United States
[6]Louis J. Fox Center for Vision Restoration, University of Pittsburgh, Pittsburgh, Pennsylvania, United States
[7]Medical Robotics Lab, College of Engineering, University of Georgia, Athens, Georgia, United States
[8]Center for the Neural Basis of Cognition, University of Pittsburgh and Carnegie Mellon University, Pittsburgh, Pennsylvania, United States
[9]Center for Neuroscience Imaging Research, Institute for Basic Science, Sungkyunkwan University, Suwon, Korea
[10]Departments of Biological Science and Biomedical Engineering, Sungkyunkwan University, Suwon, Korea
[11]Clinical and Translational Science Institute, University of Pittsburgh, Pittsburgh, Pennsylvania, United States

Correspondence: Kevin C. Chan, 3025 East Carson Street, Room 159, Departments of Ophthalmology and Bioengineering, University of Pittsburgh, Pittsburgh, PA 15203, USA; chuenwing.chan@fulbrightmail.org.

LCH and IAS contributed equally to the work presented here and should therefore be regarded as equivalent authors.

PURPOSE. The structure and biomechanics of the sclera and cornea are central to several eye diseases such as glaucoma and myopia. However, their roles remain unclear, partly because of limited noninvasive techniques to assess their fibrous microstructures globally, longitudinally, and quantitatively. We hypothesized that magic angle–enhanced magnetic resonance imaging (MRI) can reveal the structural details of the corneoscleral shell and their changes upon intraocular pressure (IOP) elevation.

METHODS. Seven ovine eyes were extracted and fixed at IOP = 50 mm Hg to mimic ocular hypertension, and another 11 eyes were unpressurized. The sclera and cornea were scanned at different angular orientations relative to the main magnetic field inside a 9.4-Tesla MRI scanner. Relative MRI signal intensities and intrinsic transverse relaxation times (T2 and T2*) were determined to quantify the magic angle effect on the corneoscleral shells. Three loaded and eight unloaded tendon samples were scanned as controls.

RESULTS. At magic angle, high-resolution MRI revealed distinct scleral and corneal lamellar fibers, and light/dark bands indicative of collagen fiber crimps in the sclera and tendon. Magic angle enhancement effect was the strongest in tendon and the least strong in cornea. Loaded sclera, cornea, and tendon possessed significantly higher T2 and T2* than unloaded tissues at magic angle.

CONCLUSIONS. Magic angle–enhanced MRI can detect ocular fibrous microstructures without contrast agents or coatings and can reveal their MR tissue property changes with IOP loading. This technique may open up new avenues for assessment of the biomechanical and biochemical properties of ocular tissues in aging and in diseases involving the corneoscleral shell.

Keywords: magic angle effect, magnetic resonance imaging, sclera, cornea, ocular hypertension

The sclera and cornea are dense connective tissues in the outer coat of the eye, which contain approximately 70% to 80% collagen by weight[1,2] with fibrils organized in lamellae.[3] Recent studies suggest an important role of the sclera and cornea in several major eye diseases such as glaucoma and myopia.[4-7] However, the roles of these tissues on the disease pathogenesis remains unclear, partly because of limited noninvasive techniques to assess and monitor their fibrous structures globally and quantitatively across time.

Magnetic resonance imaging (MRI) allows noninvasive and longitudinal monitoring of ocular structures, such as the retina[8-14] and anterior and vitreous chambers,[15-17] without depth limitation. It has also been used to image the sclera and cornea and to obtain details of ocular anatomy such as ocular shape and tissue thickness.[18-23] However, owing to the limited intrinsic MRI properties of short transverse relaxation times (T2 or T2*) in the scleral and corneal tissues, in conventional MRI sequences such as T2- or T2*-weighted imaging, the corneo-
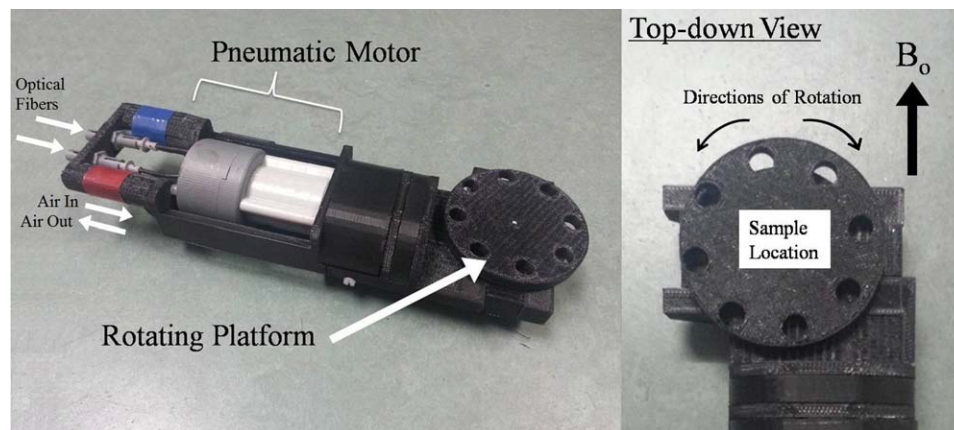
FIGURE 1. Images of the custom-made MR-compatible pneumatic automated rotating positioner used in the magic angle–enhanced MRI experiments. The *left panel* shows the general features of the rotating positioner. The *right panel* shows an enlarged top-down view of the rotating platform. Eye and tendon tissues were stabilized on the rotating platform. The angle between the tissues and the main magnetic field (B_o) was adjusted by rotating the platform driven by the pneumatic motor, using the LabView software program.

scleral shell possesses low signal intensity and appears dark in the images.[23,24] To date, the highest-resolution MRI study of the globe[19] has required exogenous contrast agents and coatings to delineate the corneoscleral shell from the dark surroundings. To the best of our knowledge, none of the techniques aforementioned has been able to visualize the internal structures of the sclera or cornea, or the effects of intraocular pressure (IOP) alterations on these tissues. Understanding the microstructures of the corneoscleral shell and their changes upon IOP loading is particularly important for resolving the recent debates on how the biomechanics and biochemistry of the fibrous corneoscleral shell may impair the nearby retina and optic nerve under ocular hypertension in glaucoma.[25,26] This may guide more targeted strategies for preserving vision from this irreversible disease, which in turn may help reduce the prevalence of this second leading cause of blindness worldwide.

The magic angle effect describes an orientation-dependent MR signal change arising when imaging highly ordered fibrous structures.[27] In highly ordered, collagen-rich fibrous tissues, such as the sclera and cornea, bounded protons are subject to dipolar interactions within a static magnetic field, which result in low T2 and T2*. The strength of these interactions depends on the angle θ between a fiber and the main magnetic field (B_o) of the MRI scanner by the term $3 \cos^2 \theta - 1$. As the dipolar interactions are minimized at $3 \cos^2 \theta - 1 = 0$, that is, when the tissues are oriented at $\theta \approx 54.7°$ or the "magic angle," the tissue MR signal intensities can be enhanced to the greatest degree and the MR sensitivity can be maximized.[27] This magic angle effect has been demonstrated extensively in MRI studies of fibrous structures in normal and diseased tendons,[28,29] menisci,[30] ligaments,[31] and cartilages[32–35] but has not yet been investigated in ophthalmic research. In this study, we hypothesized that high-field, magic angle–enhanced magnetic resonance microscopy can be used to reveal details of the fibrous structures in the corneoscleral shell, and specifically, that it can reveal the lamellar fibers and the waviness, or crimp, of the collagen fibers that form the corneoscleral shell. Further, we hypothesized that the high sensitivity of magic angle effect to the structural alignment of the collagen fibers would improve the detection of the MRI signal differences in ocular tissues between no-load and elevated IOP conditions. In addition, we evaluated the intrinsic MR tissue properties in terms of the absolute transverse relaxation time constants, T2 and T2*, of the sclera and cornea by using T2 and T2* mapping to characterize quantitatively the extents of magic angle effect

on different types of MR images in both loaded and unloaded tissues.

MATERIALS AND METHODS

Tissue Preparation

Nine pairs of ovine eyes were obtained from the local abattoir and processed within 12 hours of death. The eyes were divided into two groups. In group 1, four eyes from two ovines were immersion fixed with 10% formalin without cannulation and then washed in phosphate-buffered saline (PBS). The eyes then underwent whole-globe MRI followed by sectioning of the sclera and cornea for high-resolution magic angle–enhanced MRI. These sections were 2- to 5-mm thick, made by manually cutting in the superior–inferior direction by using a razor. Section location varied, depending on the region to be imaged, namely, cornea and anterior or posterior sclera. In group 2, one eye from each of the remaining seven ovines was loaded at an IOP of 50 mm Hg by using a gravity perfusion fixation system and a cannula inserted into the anterior chamber (Jan NJ, et al. *IOVS* 2013;54:ARVO E-Abstract 65; Sigal et al. *IOVS* 2013;54:AR-VO E-Abstract 3158). The contralateral eyes were cannulated but not pressurized. All eyes were then immersion fixed with 10% formalin, washed in PBS, and dissected with razors and surgical scissors to isolate the sclera and cornea. Similarly, 13 ovine Achilles tendons from the same set of animals were also washed in PBS and dissected to isolate thin strips and act as positive controls of the ocular tissues, given the well-known magic angle effect in tendon and the similar structural compositions between the tendon and corneoscleral shell. Four strips were randomly selected and were loaded by using alligator clips attached to a rod to keep stretched, followed by immersion fixation with 10% formalin. The remaining nine strips were fixed but unloaded. Three loaded tendons and seven unloaded tendons underwent the same MRI scans as the ocular tissues in groups 1 and 2. In addition, one of the unloaded tendons was placed in a glass test tube, such that the tendon strip made a "U-shape" at the bottom of the test tube to illustrate how the MR signal enhancement affected the visualization of collagen fiber crimp structures at different angles continuously from 0° to 90° to B_o. The test tube was filled with 10% formalin and fixed overnight. Afterwards, the formalin was replaced with PBS, and high-resolution MRI was performed to the U-shaped tendon. The remaining one loaded
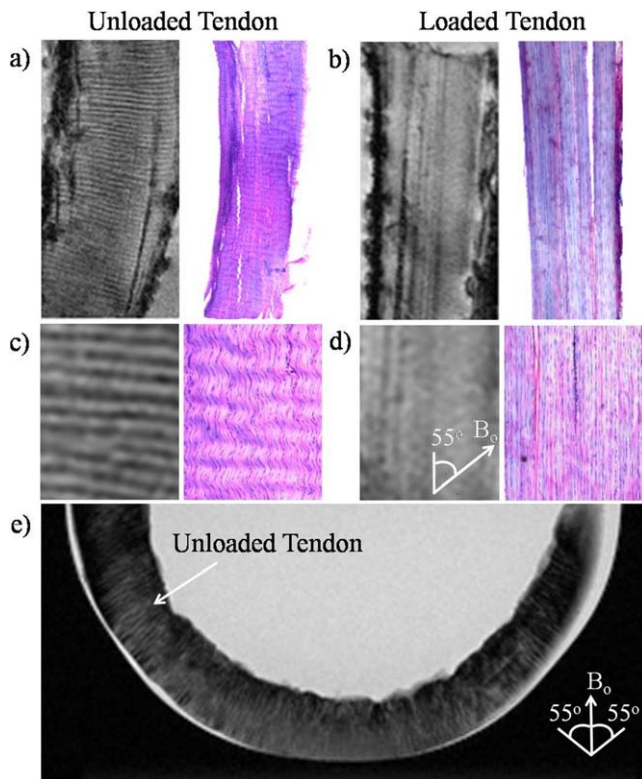
FIGURE 2. Illustrations of collagen fiber crimps in magic angle–enhanced MRI and histology, using tendons with and without loading. (**a**, **b**) High-resolution T2*-weighted MR images of unloaded ([**a**]: *left*) and loaded ([**b**]: *left*) tendons oriented at the magic angle at approximately 55° to the main magnetic field (B_o) (repetition time = 3 s; echo time = 5 ms; in-plane resolution = 27×27 μm²), and light microscopy of H&E staining in unloaded ([**a**]: *right*) and loaded ([**b**]: *right*) tendons at ×4 magnification under bright field. As seen in the enlarged views (**c**, **d**) of the corresponding images in (**a**, **b**), the collagen fiber crimps were revealed as wavy structures by H&E staining in the unloaded tendon, whereas the fibers appeared to be straightened in the loaded tendon. Similar light/dark banding arrangement was observed in T2*-weighted MR images in the unloaded tendon but not loaded tendon. (**e**) T2-weighted MR image of a U-shaped unloaded tendon positioned at the bottom of a test tube (repetition time = 3 s; echo time = 11 ms; in-plane resolution = 78×78 μm²). Magic angle signal enhancement effect could be observed when the tendon tissues were oriented near the magic angle. The collagen fiber crimps were also more clearly distinguished when the tissues were oriented near the magic angle compared with 0° or 90° to B_o.

and one unloaded tendons were taken for histologic evaluations of the collagen fiber crimps. They were cut into ~3-mm-thick and ~1-cm-long strips and processed in 30% sucrose. The strips were then embedded and frozen in cryogel and cryosectioned into 50-μm sections. These sections were washed with water, ethanol, and xylene, stained with hematoxylin-eosin (H&E), and mounted by using Permount.

MRI Protocol

Eye and tendon tissue samples were suspended in agarose gel to prevent vibrational movement during imaging and were scanned by using a 9.4-Tesla/31-cm Varian/Agilent horizontal MRI scanner (Varian/Agilent, Santa Clara, CA, USA). Tissue samples were positioned relative to B_o by using a custom-made MR-compatible pneumatic automated rotating positioner (Fig. 1).[36] In group 1, the whole globe of the intact eye was positioned and scanned at several orientations to the main

magnetic field (B_o) inside the scanner by using T2*-weighted gradient-echo imaging at voxel size of $60 \times 60 \times 800$ μm³ with a 38-mm-diameter transmit–receive volume coil. For high-resolution microstructural evaluation of tissue sections in group 1, the tissues were orientated at 55° relative to B_o inside the scanner, and T2*-weighted gradient-echo pulse sequences were applied at 16×16 μm² to 27×27 μm² in-plane resolution, 400-μm to 700-μm slice thickness, 3-s repetition time, and multiple echo times by using a custom-made 12-mm-diameter transmit–receive surface coil. The magic angle effect of the same tissues was also evaluated by examining the relative signal intensities at different angular orientations from 0° to 90° relative to B_o, using the same gradient-echo MRI scanning protocol at 30×30 μm² in-plane resolution, 500-μm slice thickness, 3-s repetition time, and 5-ms echo time. For comparisons of the absolute MR transverse relaxation times between loaded and unloaded tissue samples in group 2, T2 and T2* mapping with spin-echo and gradient-echo MRI pulse sequences was respectively performed by using a custom-made 25-mm-diameter transmit–receive surface coil. The loaded and unloaded eye and tendon tissue samples were paired up and positioned at the same angular orientations as in group 1. The MRI parameters were as follows: (1) spin-echo sequence: repetition time/echo time = 1000/9.7 ms; echo space time = 9.7 ms; number of echoes = 3; (2) gradient-echo sequence: repetition time/echo time = 1000/2.9 ms; echo space time = 3.4 ms; number of echoes = 3. For both spin-echo and gradient-echo sequences in group 2, in-plane resolution = 110×110 μm² and slice thickness = 1 mm.

Data Analysis

The MR images were reconstructed by using ImageJ software v1.47 (http://imagej.nih.gov/ij/; Wayne Rasband, provided in the public domain by the National Institutes of Health, Bethesda, MD, USA) for qualitative evaluation of morphologic details in the sclera, cornea, and tendon. For quantitative data analyses of relative T2- and T2*-weighted signal intensities as well as absolute T2 and T2* MR transverse relaxation times, regions of interest were manually drawn on the eye and tendon tissues in the spin-echo and gradient-echo MR images, respectively, by using ImageJ to extract the signal intensities at different echo times and angles to B_o. Intrinsic T2 and T2* values of the loaded and unloaded tissues were derived from curve fitting of T2- and T2*-weighted signal decays, respectively, with at least two echo times by using the equations $S_{SE}(TE) = S_{SE}(0)e^{(-TE/T2)}$ and $S_{GE}(TE) = S_{GE}(0)e^{(-TE/T2^*)}$, or $T2 = (TE_2 - TE_1)/\{ln[S_{SE}(TE_1)] - ln[S_{SE}(TE_2)]\}$ and $T2^* = (TE_2 - TE_1)/\{ln[S_{GE}(TE_1)] - ln[S_{GE}(TE_2)]\}$, where S_{SE} and S_{GE} are the signal intensities (S) from spin-echo (SE) and gradient-echo (GE) MR images at a particular echo time (TE). Results are presented as mean ± standard deviation. Measurements between loaded and unloaded tissues, and between 0° and 55° to B_o were compared with Student's *t*-tests. One-tailed tests were used to confirm prior findings[37] that loaded tendons would possess longer transverse relaxation times than unloaded tendons at the magic angle under similar MRI settings. Elsewhere, two-tailed tests were used. Results were considered significant when $P < 0.05$.

RESULTS

Figure 2 illustrates how the magic angle phenomenon affects the visualization of collagenous crimp structures in the tendon-positive control, and how this changes with loading. As shown in Figures 2a through 2d, the collagen fiber crimps were revealed as wavy structures by H&E staining in the unloaded tendon, whereas these fibers appeared to be straightened in the loaded tendon. Similar light/dark banding arrangement was
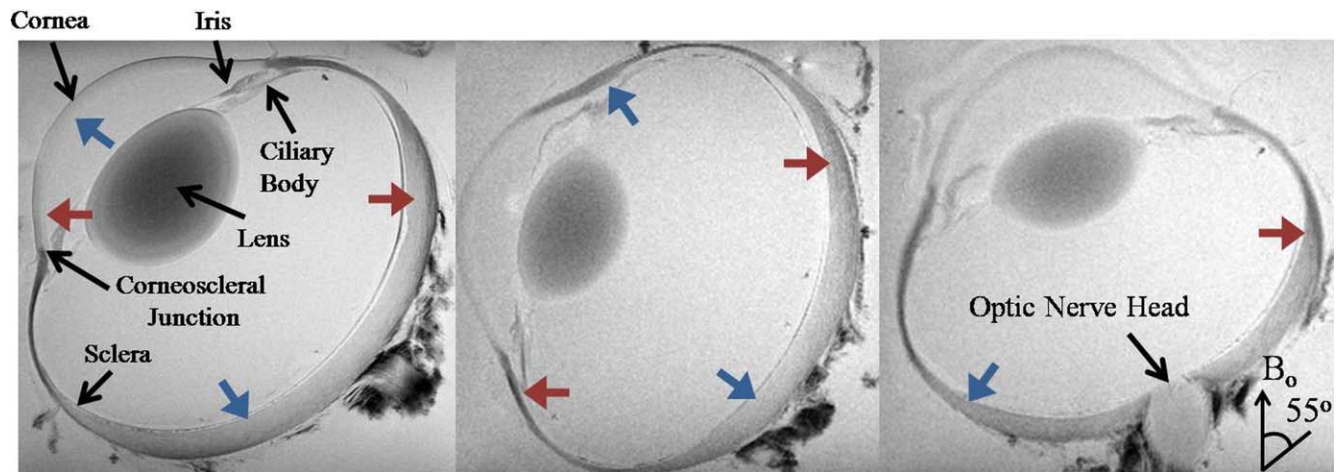
FIGURE 3. Representative T2*-weighted MR images of a sheep eye at three different orientations to the main magnetic field (B_o). Note the signal enhancement in the corneoscleral shell when the fiber orientation was near the magic angle at approximately 55° relative to the B_o direction (*blue arrows*) compared to approximately 0° relative to B_o direction (*red arrows*) (repetition time = 3 s; echo time = 4 ms; in-plane resolution = 60 × 60 μm^2).

observed in high-resolution T2*-weighted MR images in the unloaded tendon but was not visible in loaded tendon when tissues were oriented at the magic angle at approximately 55° to B_o. In the T2-weighted MR image of a U-shaped unloaded tendon (Fig. 2e), the light/dark bands of collagen fiber crimps were more clearly distinguished when the tissues were oriented near the magic angle compared with 0° or 90° to B_o. Note also the magic angle signal enhancement effect when the tendon tissues were oriented near the magic angle.

Within the eyeball, magic angle–enhanced MRI revealed distinct microstructural details and differential signal enhancement of the fibrous structures in the normal, unpressurized ocular tissues in group 1. As shown in Figure 3, typical T2*-weighted MR images of a normal, unpressurized ovine eye illustrated the signal enhancement in the corneoscleral shell when the fibers were oriented toward the magic angle at approximately 55° relative to B_o. Comparing between ocular tissues and the tendon, T2*-weighted MR images in Figure 4a reveal the light/dark banding arrangement in both tendon and anterior sclera when they were oriented near the magic angle, indicative of the collagen fiber crimp structures. The lamellar fibers along the outer and inner layers of the anterior sclera, posterior sclera, and cornea were also distinguished. Figure 4b illustrates the T2*-weighted MR images of the unloaded sclera around the optic nerve head. Details of the lamina cribrosa within the optic nerve head and the distributions of crimps in the surrounding scleral fibers were revealed especially at orientations near the magic angle.

Using the MRI-compatible pneumatic automated rotating positioner (Fig. 1), the unloaded tendon, sclera, and cornea were oriented at different angles to B_o and were found to experience different extents of magic angle MR signal enhancement (Fig. 5a). All three tissues possessed maximum signal intensities in T2*-weighted MR images when they were oriented about the magic angle at 55° to B_o (Fig. 5b). The magic angle enhancement was found to be the strongest in the tendon (186% ± 34% at 55° relative to 0° to B_o) and the least strong in the cornea (23% ± 5% at 55° relative to 0° to B_o), whereas the sclera was enhanced by 82% ± 1% about the magic angle compared to 0° to B_o.

Biomechanical loading of the tendon and ocular tissues caused increases in relative MR signal intensities as well as absolute MR transverse relaxation times when the tissues were oriented near the magic angle (Figs. 6–8). In Figure 6a, T2- and

T2*-weighted MR images of unloaded tendon at the magic angle revealed some crimp patterns as observed in Figure 4 even under a lower in-plane resolution at 110 × 110 μm^2. Loaded tendon appeared to show higher intensities than unloaded tendon in both T2- and T2*-weighted MR imaging at magic angle. However, the collagen fiber crimps were less apparent in loaded tendon. Figure 6b shows the echo time–dependent T2- and T2*-weighted signal decay curves of loaded and unloaded tendons at the magic angle. T2 and T2* MR transverse relaxation times were derived from curve fitting of the slopes of the logarithmic signal decay curves given their inversely proportional relationships. At the magic angle, intrinsic T2 (41.2 ± 8.7 ms) and T2* (14.8 ± 8.7 ms) values of the loaded tendon were significantly higher than those of the unloaded tendon (T2 = 29.7 ± 6.0 ms and T2* = 7.1 ± 1.8 ms) (one-tailed unpaired *t*-tests: $P < 0.05$). Figure 7 shows the T2- and T2*-weighted MR images of representative loaded and unloaded pairs of sclera (Figs. 7a, 7b) and cornea (Figs. 7c, 7d) at 0°, 55°, and 90° to B_o under identical MRI acquisition parameters as the tendon in Figure 6. Magic angle signal enhancement was observed in both loaded and unloaded ocular tissues, with the magic angle effect on loaded tissues being apparently stronger than on the unloaded tissues. Quantitative comparisons of the absolute MR transverse relaxation times in Figure 8 confirmed these findings and showed that the intrinsic T2 and T2* values of the sclera (Fig. 8a) and cornea (Fig. 8b) were generally higher in loaded than unloaded conditions at most orientations, whereas statistical significance was reached when loaded and unloaded tissues were oriented near the magic angle (two-tailed paired *t*-tests: $P < 0.05$).

DISCUSSION

Our results support the hypothesis that high-field magic angle–enhanced MR microscopy can reveal details of the fibrous structures in the ocular tissues without the need for exogenous contrast agents or coatings. Our technique relied on the use of the magic angle effect that has been observed clinically in MRI studies of fibrous tissues such as tendon[28,29] and cartilage.[32–35] Further, our results showed that this imaging technique can improve the detection of the differences between unloaded and loaded ocular tissues in relative T2- and T2*-weighted MR signal intensities as well as absolute T2 and T2* MR transverse
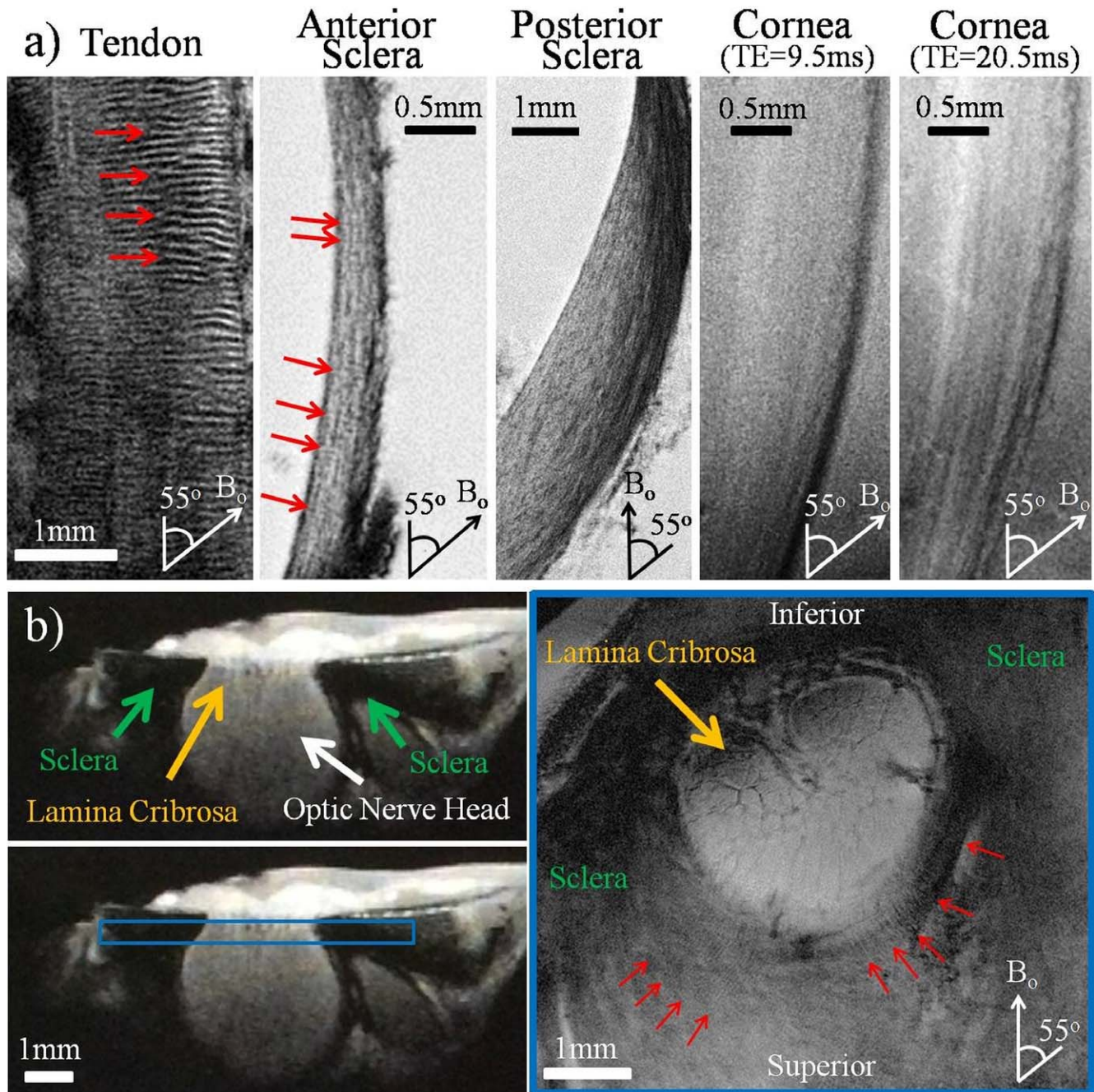
FIGURE 4. (a) High-resolution T2*-weighted MR images of the normal unloaded tendon, anterior sclera, posterior sclera, and cornea positioned at the magic angle at approximately 55° to the main magnetic field (B_o). Collagen fiber crimps (*red arrows*) were observed in the tendon positive control and the anterior sclera. Lamellar fibers were observed along the anterior and posterior sclera, whereas differential image contrasts were found across corneal layers at echo times of 9.5 and 20.5 ms. Outer layers are to the *right* in the sclera and cornea images. Repetition time for all tissues = 3 s; echo time of tendon, anterior sclera, and posterior sclera = 8, 9.5, and 8 ms, respectively; in-plane resolution of tendon, anterior sclera, posterior sclera, and cornea = 20 × 20, 16 × 16, 20 × 20, and 16 × 16 μm², respectively. (**b**) T2*-weighted MR images of the unloaded sclera near the optic nerve head. The *left panels* show the cross-section of the sclera, optic nerve head, and lamina cribrosa in sagittal view. The *right panel* shows the coronal T2*-weighted image oriented as the *blue box* in the *left panel* at 16 × 16 μm² in-plane resolution and repetition time/echo time = 3000/9.5 ms. Details of the lamina cribrosa (*yellow arrow*) within the optic nerve head and the distributions of crimps (*red arrows*) in the scleral fibers surrounding the optic nerve head were revealed especially at orientations near the magic angle.

relaxation times. Upon magic angle enhancement, significantly larger MR tissue relaxivity differences between unpressurized and pressurized eyes were observed in the sclera and cornea. Thus, it may be possible to apply the magic angle effect to improve sensitivity for MRI studies of the corneoscleral shell in normal and diseased conditions such as glaucoma.

In this study, high-resolution magic angle–enhanced MRI was shown to be feasible for revealing tissue microstructures of the corneoscleral shell, including banding indicative of collagen fiber crimp. The crimps arise from ordered collagenous fibers that follow zig-zag[38–40] or helicoidal[41] patterns in the tendon and ocular tissues, respectively, and act as a functional biomarker of
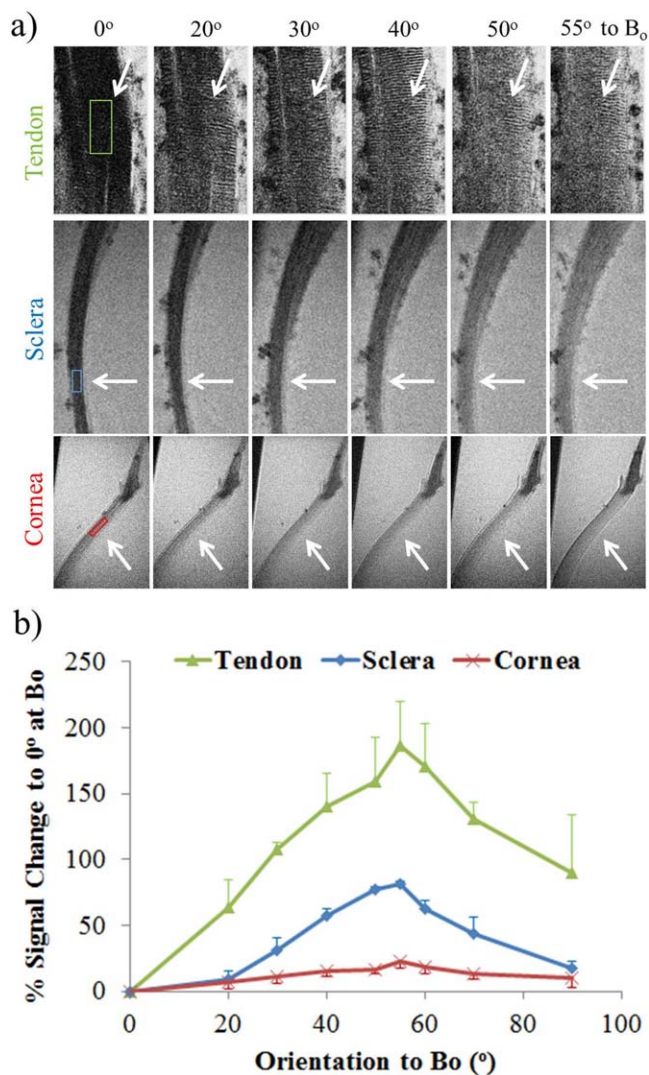
FIGURE 5. (a) Qualitative and (b) quantitative assessments of the magic angle effect on relative T2*-weighted signal intensities (mean ± standard deviation) in normal unloaded tendon, anterior sclera, and cornea (*white arrows*). The tissues were oriented at nine angles from 0° to 90° with respect to the main magnetic field (B_o). Maximum signal intensity was found for all three tissues at the magic angle at approximately 55° to B_o (two-tailed paired *t*-tests between 0° and 55°, $P < 0.05$). The tendon had the largest signal enhancement by 186% ± 34% at the magic angle relative to 0°, whereas the cornea had the smallest increase by 23% ± 5% ($P < 0.05$ between tissues). The sclera was enhanced by 82% ± 1% about the magic angle (repetition time = 3 s; echo time = 5 ms; in-plane resolution = 30 × 30 μm²).

tissue strain.[38,39,42,43] These complex collagen structures have been observed as banding patterns in light microscopy[38,39,44,45] and MRI[37,45] in the normal, unloaded tendons (Fig. 2). Similar crimping patterns are shown in Figure 4 of the current study by magic angle–enhanced MRI in the scleral fibers anterior and adjacent to the lamina cribrosa. The crimps observed in the sclera could also be a biomarker to help understand the load-bearing and tissue strain in the eye. Apart from collagen fiber crimps, lamellar fibers are clearly visible in the MR images of the anterior and posterior sclera, which may reflect the interwoven arrangement of collagen bundles across the scleral layers. The corneal stroma, which occupies approximately 90% of total corneal thickness, also consists of lamellar collagen fibers that are visible by MRI at the magic angle in Figure 4. On the other

hand, there is a rich water content in the corneal stroma and to a lesser extent in the sclera.[46,47] The difference in tissue water composition might explain the lower background MR signal intensities and the smaller T2 and T2* values of the sclera relative to the cornea at all measured orientations throughout the study. The superficial layers of the corneal stroma contain more traversing fibers[48,49] and proteoglycans, which possess high water-binding capacity,[50] and possibly lower T2 and T2* than the deeper layers. In addition, the corneal epithelium above the fibrous corneal stroma is mainly composed of dense cellular layers,[51] which may not readily possess magic angle enhancement effect in MRI. These might explain the graded signal intensity increase from the superficial layers to the deeper layers of the cornea in our MR images.

The tendon, sclera, and cornea were found to experience different extents of magic angle signal enhancement effect in the normal, unloaded conditions, possibly due to their differential biochemical compositions and microstructural fiber organizations.[52] The tendon has close to 100% collagen by dry mass,[53] whereas the sclera and cornea contain less collagen content of approximately 80% and 70% by dry weight, respectively,[1,2] with more complex structures of proteoglycans and glycoproteins.[54] The smaller magic angle effect in the sclera and cornea than the tendon can be expected given a smaller decrease in dipole–dipole interactions from a lesser amount of existing collagen fibers in the ocular tissues at the magic angle. In addition, the collagen fibrils in the tendon are generally aligned parallel to its long axis, whereas those in the corneoscleral shell are arranged in slightly different directions and may traverse each other across the lamellar structures to provide maximum mechanical strength within the curved globe.[5,49,52,54,55] Such traverse fibers are particularly predominant in the outer cornea compared to the inner cornea.[48,49] When the collagen fibers are not arranged in parallel, such as in the ocular tissues, the magic angle effect of some fibers oriented at the magic angle in an image voxel may be smeared by fibers oriented at other directions within the same voxel, resulting in a smaller net magic angle effect in the sclera and cornea compared to the tendon, and thus the weaker signal enhancement in Figure 5 of the current study. On the other hand, even though ocular tissues are similar to tendon in terms of extracellular matrix composition, there are some differences in their structural hierarchies. For example, unlike tendon, corneal and scleral collagen contains no fascicular order of structure and demonstrates a more oblique molecular tilt with respect to the fibril axis (~15° in the cornea versus ~4° in the tendon).[52] Although this molecular tilt has been suggested to result in lower axial periodicity of microfibrils in cornea compared to tendons,[52] the consequences of this tilt on our MRI results are unclear. We did not detect an apparent deviation of angle at maximum signal enhancement from the magic angle at 55° to B_o between tissues. Whether this tilt may have contributed to the lower magic angle effect strength in ocular tissues compared with tendon will be the subject of further investigation.

From the results in Figures 7 and 8, upon acute ocular hypertension, apparent increases in T2- and T2*-weighted signal intensities and significant T2 and T2* lengthening were observed in the loaded sclera and cornea compared to unloaded ocular tissues near the magic angle. These observations were similar to those in the loaded and unloaded tendon control MRI experiments in Figure 6 as well as a recent tendon MRI study under the same magnetic field strength.[37] The increases in signal intensities and MR transverse relaxation times might be due to the realignment of the collagen fibers, such as decrease in waviness of fiber crimps (Sigal et al. *IOVS* 2013;54:ARVO E-Abstract 3158)[56] and reorientation of scleral and corneal lamellar fibers[3,49-51] upon stretch and compression.[5,57-59] Down to the atomic level, it could also reflect the fiber protons being moved further apart, resulting in diminishing spin
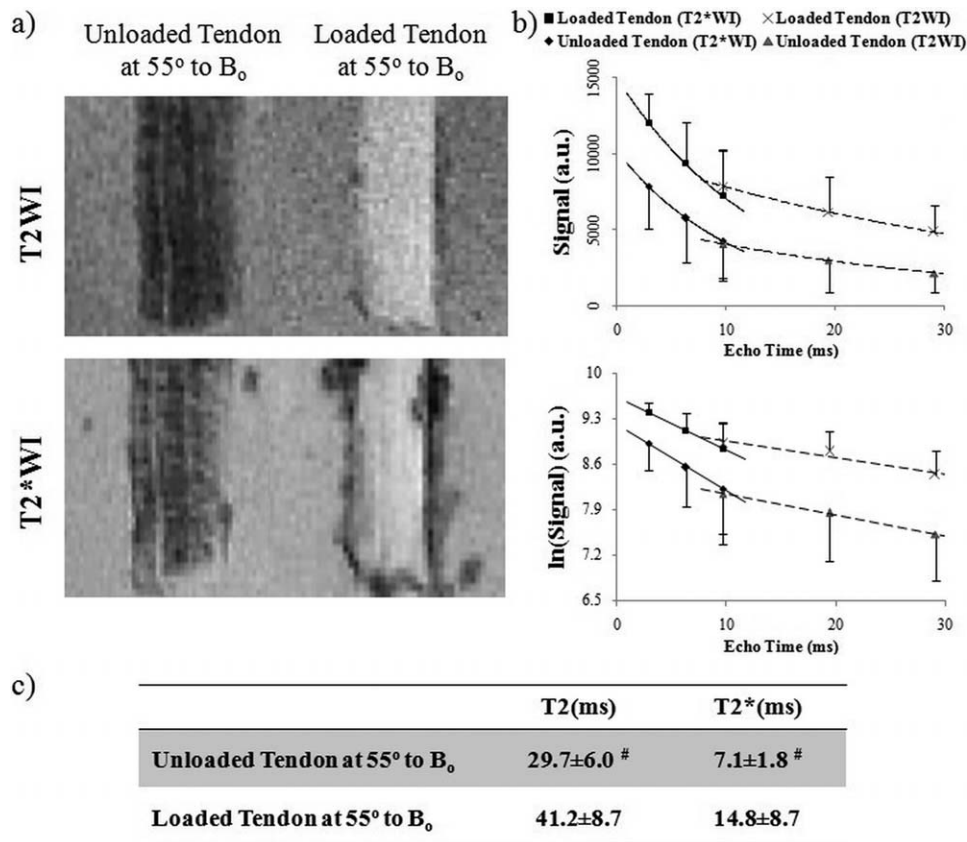
FIGURE 6. (a) T2-weighted (T2WI) and T2*-weighted MR images (T2*WI) showing the unloaded and loaded tendon controls at the magic angle at approximately $55°$ to the main magnetic field (B_o) with repetition time/echo time = 1000/9.7 ms and in-plane resolution = 110×110 μm^2. The signal intensity in the loaded tendon was found to be higher than unloaded tendon in all samples. (b) Echo time–dependent T2- and T2*-weighted signal decay curves of the loaded and unloaded tendons at the magic angle with and without logarithmic scaling (mean ± standard deviation) for deriving the intrinsic MRI tissue properties in terms of absolute transverse relaxation time constants (T2 and T2*) using the equations $S_{SE}(TE) = S_{SE}(0)e^{(-TE/T2)}$ and $S_{GE}(TE) = S_{GE}(0)e^{(-TE/T2*)}$, or T2 = $(TE_2 - TE_1)/\{\ln[S_{SE}(TE_1)] - \ln[S_{SE}(TE_2)]\}$ and T2* = $(TE_2 - TE_1)/\{\ln[S_{GE}(TE_1)] - \ln[S_{GE}(TE_2)]\}$. Note the inverse proportionality between MR transverse relaxation time and the slope of the logarithmic signal decay curve. (c) Table comparing intrinsic T2 and T2* values between loaded and unloaded tendons at the magic angle. Significant T2 and T2* lengthening was found in the loaded tendon compared to unloaded tendon (one-tailed unpaired *t*-tests: #$P < 0.05$). Note the lower spatial resolution used in the current images compared with the images of Figure 2, which limited direct visualization of the bands corresponding with crimp.

dephasing between neighboring protons.[37] The absolute T2 and T2* differences between loaded and unloaded ocular tissues were found to be more pronounced near the magic angle, indicative of the sensitivity boost offered by the magic angle effect in eye-related MRI research. At $0°$ to B_o, loaded sclera, but not cornea, tended to possess slightly higher T2 and T2* than unloaded tissues without reaching statistical significance ($P = 0.26$). Since long repetition times (1–3 s) and short echo times (2.9–9.7 ms for gradient-echo; 9.7–29.1 ms for spin-echo) were used in some MRI sequences in this study, it is possible that some of the MR images were relatively more proton-density weighted, and the signal intensity differences between tissues could be partially contributed from water proton density effect. However, given that the measured T2 and T2* of unloaded tendon (~30 ms and ~7 ms, respectively, at magic angle), sclera (~15 ms and ~5 ms, respectively, at $0°$ to B_o), and cornea (~30 ms and ~17 ms, respectively, at $0°$ to B_o) were close to the echo times used in this study, and that the optimal echo time for detecting a maximal signal in T2- and T2*-weighted imaging is at approximately T2 and T2*,[60] our images shown in this study are expected to possess significant T2 and T2* weighting and magic angle–induced T2 and T2* effects. We would also like to note that the signal-to-noise ratios of the images have been carefully assessed and were observed to be sufficient for T2 and T2* quantitation using the current MRI

sequences in Figures 6 and 8. Future studies will investigate the relative contributions of water, collagen, and other macromolecules to the signal sources of loaded and unloaded tissues, using biophysical modeling and multimodal MRI assessments.

The corneoscleral shell structure has been studied extensively[52,55] by using atomic force microscopy,[61] transmission[62] and scanning electron microscopy,[63] and light microscopy with[4] or without immunohistochemistry (Jan NJ, et al. *IOVS* 2014;55:ARVO E-Abstract 3715 and Ref. 48). Collagen fiber organization has also been measured by using small-angle light scattering[64] and small- and wide-angle x-ray scattering,[52,55] and predicted numerically by using inverse modeling.[56] These techniques have excellent resolution and sensitivity, which our MRI-based technique cannot match. There is also extensive knowledge based on the use of labels, dyes, and contrast agents that enhance the capabilities of microscopy of sclera and cornea, and these agents are only starting to be developed for MRI. However, unlike MRI, most of these techniques are invasive or destructive, which hinder multimodality assessments on the same sample, or in vivo applications without substantial sample manipulation. In addition, although an increasing number of studies have suggested the involvement of the fibrous corneoscleral shell in retina and optic nerve impairments under chronic ocular hypertension or glaucoma,[25,26,65] most of these studies have been performed ex vivo
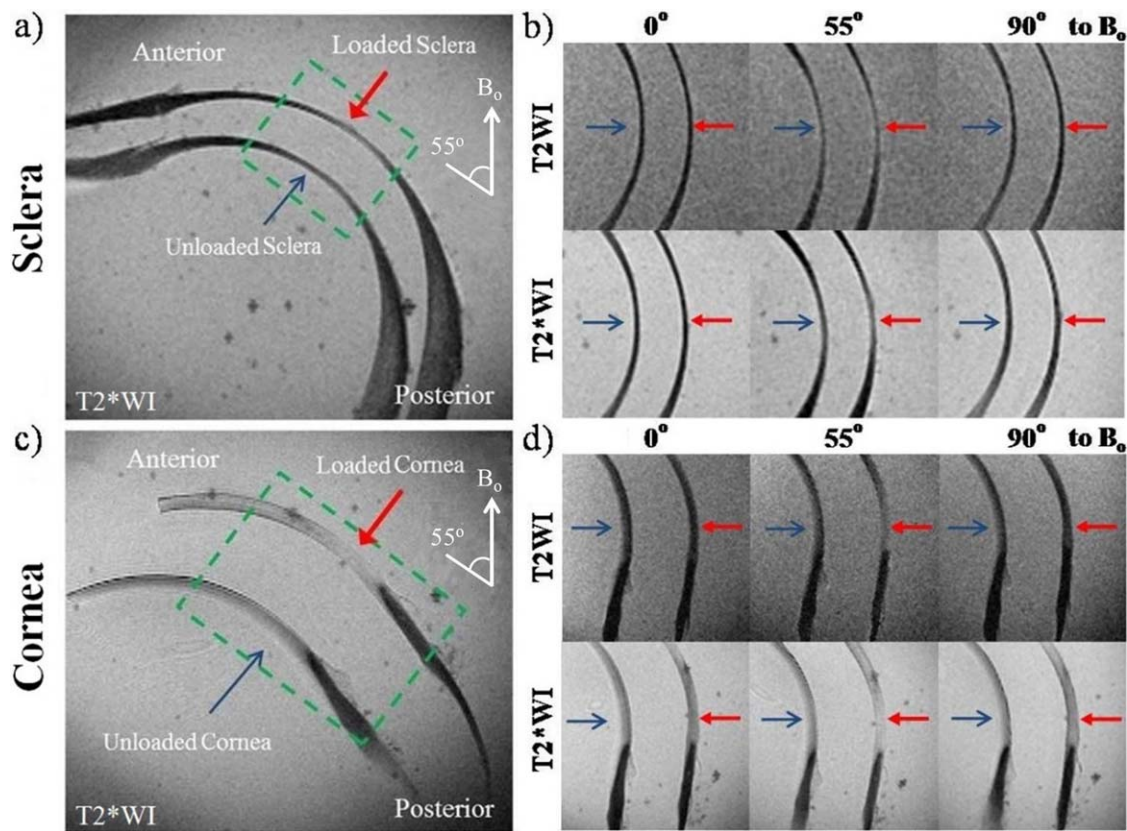
FIGURE 7. (a, c) T2*-weighted MR images (T2*WI) of the unloaded (*blue arrow*) and loaded (*red arrow*) sclera (a) and cornea (c) tissue sections at the magic angle at approximately 55° to the main magnetic field (B_o); (b, d) T2-weighted images (T2WI) and T2*WI of the sclera (b) and cornea (d) enlarged from the *green dashed boxes* in (a, c) when the ocular tissues were oriented and scanned at 0°, 55°, and 90° to B_o under the same MRI acquisition parameters as the tendon controls in Figure 6. Magic angle signal enhancement was observed in both T2WI and T2*WI of the sclera and cornea. Stronger signal enhancement was observed in the loaded tissues than unloaded tissues (repetition time = 1 s; echo time = 9.7 ms; in-plane resolution = 110×110 µm^2).

or through numerical simulation and the underlying mechanisms remain debatable. Our imaging technique allowed us to obtain information on the load-bearing connective tissues of the cornea and sclera without the need for sectioning, staining, labeling, or 3-D structure alignment, which are typical for the study of the eye. The images had larger field of view and increased penetration depth than observed with common tools used to study the eye, such as optical coherence tomography. Also, unlike optical coherence tomography, which requires a clear central visual axis for imaging of the bases of the eye, MRI does not require light sources and can be readily applied to assess patients with obstructed visual axis such as cataract, which commonly coexists with glaucoma in the elderly population. Although the signal intensities in T2- and T2*-weighted imaging are relative to systems' settings, image contrast, and magnetic field homogeneity, and are not translatable across scanners, the intrinsic T2 and T2* transverse relaxation time constants derived from T2 and T2* mapping are absolute values comparable across scanners in different experimental sessions, and hold promise as reliable, noninvasive biomarkers to allow in-depth and longitudinal assessments for future eye-related magic angle–enhanced MRI research. Future studies may apply the current magic angle–enhanced MRI technique to elucidate how graded IOP increases may alter the intrinsic T2 and T2* values as well as the lamellar and crimp fiber arrangements in the sclera and cornea, and how acute and chronic IOP increases and sustained reduction of elevated IOP, mimicking glaucoma treatment, may affect tissue remodeling and intrinsic T2 and T2* contrasts in the corneoscleral shell.

Future studies may also use the magic angle effect to enhance other intrinsic MRI contrasts, such as T1ρ,[66,67] magnetization transfer,[68] and chemical exchange saturation transfer,[69,70] for examining different biochemical compositions, including collagen and proteoglycans, within the ocular tissues in health and disease.

The results we presented shall be interpreted by considering several limitations. Voxel size, while excellent for MRI studies of the eye, was still larger than some aspects of tissue microstructure of interest. Measurements of collagen fiber crimps in the eye, using higher-resolution optical imaging, suggest that this may be the reason why the crimps were not as clearly visible in some regions of the sclera (Sigal et al. *IOVS* 2013;54:ARVO E-Abstract 3158) or were even not visible in the cornea (Jan NJ, et al. *IOVS* 2014;55:ARVO E-Abstract 3715). The collagen fiber crimp period on average has been shown to be the largest in tendon, followed by sclera and cornea (Sigal et al. *IOVS* 2013;54:ARVO E-Abstract 3158; Jan NJ, et al. *IOVS* 2014;55:ARVO E-Abstract 3715). In addition, crimps in sclera and cornea are not as uniformly distributed as in tendon. Given the in-plane resolution of MR images of sclera at 16×16 µm^2 and cornea at 20×20 µm^2 in Figure 4, only the crimps with periods larger than 2 voxels are expected to be distinguishable, or else the smaller crimps would be susceptible to partial volume effect. We propose that the combined use of the higher resolution of optic systems, such as optical coherence tomography, and the larger field of view, penetration depth, and multimodal tissue property assessments of MRI may provide important complementary information of the corneo-

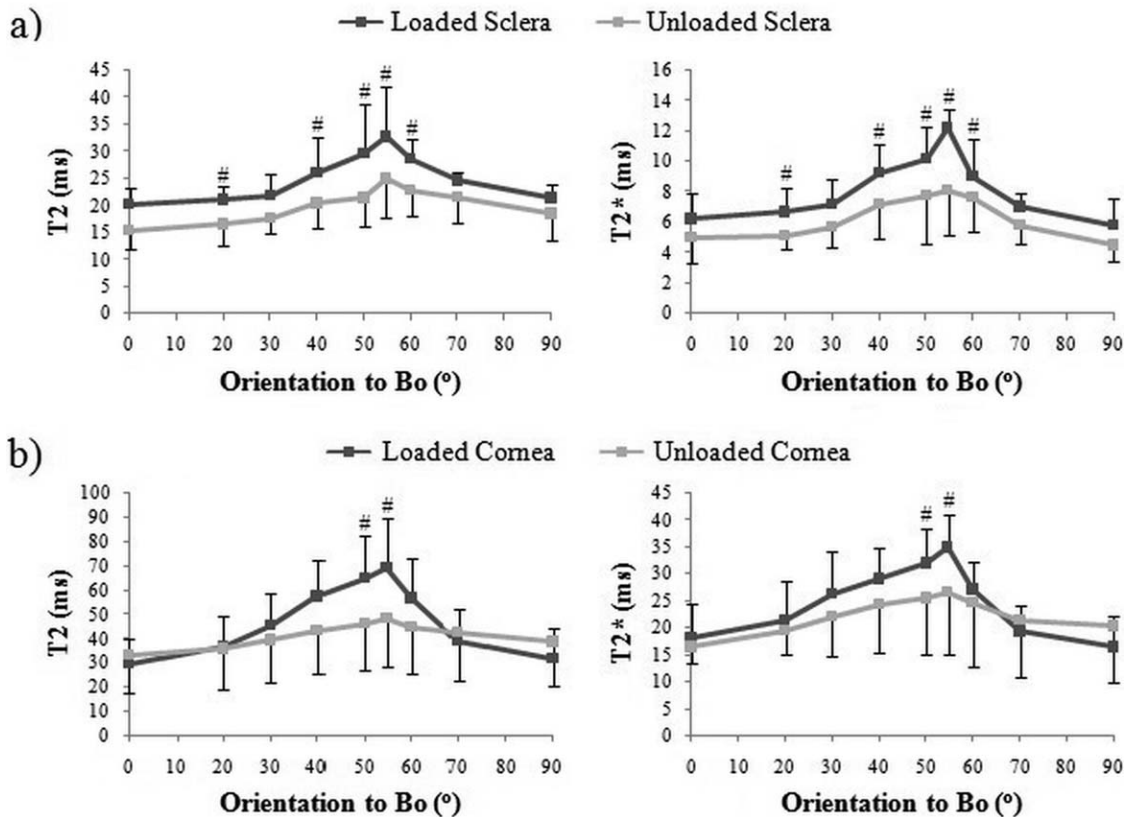## Transverse Relaxation Times of Loaded and Unloaded Ocular Tissues

FIGURE 8. Plots of absolute MR transverse relaxation times (T2 and T2*) (mean ± standard deviation) in the loaded and unloaded sclera (**a**) and cornea (**b**) when the tissues were oriented at nine different angles from 0° to 90° relative to the main magnetic field (B_o). The intrinsic T2 and T2* values appeared to maximize at 55° to B_o in both loaded and unloaded ocular tissues. Significantly larger T2 and T2* increases were observed in loaded ocular tissues than in unloaded tissues near the magic angle (two-tailed paired t-tests between loaded and unloaded tissues: #$P < 0.05$).

scleral shell in future studies. On the other hand, the tissues studied in this work were fixed. This is routine in the study of collagen structure and crimp when using histology or in MRI,[37] and it has been demonstrated that, in tendons, collagen fiber crimp is robust to fixation even after overnight fixation.[37,39,71] Fixation, however, may alter the relaxation parameters, and we made the same assumption as that of a previous tendon MRI study that the effects of chemical fixation on relaxation times were similar between loaded and unloaded tissues.[37] We opted to fix the tissues to avoid potential motion artifacts or variability in applying constant loading on fresh tissues simultaneously during imaging at different orientations, which is nontrivial inside the small-bore of a large magnet. We should point out that the eyes were not processed in ethanol, plastic, or paraffin as is often the case following fixation, and therefore did not suffer the substantial shrinkage often associated with tissue processing.

Our goal in this article was to demonstrate the feasibility of the magic angle–enhanced MRI technique in the corneoscleral shell, as a step toward the long-term objective of a clinical application in the eye. Given the widespread application of MRI clinically and the fact that our technique shares similar physical principles in both high-field MRI and clinical MRI, we believe that this remains a possibility. Nevertheless, we want to emphasize that several technical challenges remain to be overcome. These include the limited spatial resolution of a clinical scanner, the short MRI scan time possible in a clinic, and image artifacts from eye motion during imaging. These

challenges are continually being addressed, for example, by optimizing MRI hardware settings, or developing gaze fixation schemes that improve image quality at submillimeter resolution within clinically acceptable scan time (Stachs O, et al. *IOVS* 2014;55:ARVO E-Abstract 5843 and Refs. 72–74). Further work is also needed to refine the sensitivity of our technique to detect more subtle differences in MR signals that are likely to be associated with more graded pressure differences in both young and aged human eyes in nonfixed fresh tissues or in vivo.

CONCLUSIONS

We demonstrated the feasibility of using magic angle–enhanced MRI for imaging of the microstructures of fibrous ocular tissues, such as lamellar fibers and crimps, at high spatial resolution. It can also be used to quantify and differentiate MR tissue relaxivity changes upon IOP loading. T2- and T2*-weighted signal intensities were found to be maximal when the sclera and cornea were oriented near the magic angle at approximately 55° to B_o. More pronounced magic angle signal enhancement was found in loaded than unloaded ocular tissues, suggestive of the changes in collagen fiber crimp and alignment. Absolute T2 and T2* MR transverse relaxation times were significantly higher in loaded than unloaded sclera and cornea when the tissues were oriented near the magic angle but not at 0° to B_o, indicative of the sensitivity boost offered by the magic angle effect for eye-

related MRI research. We demonstrated a promising technique that may open up new avenues of noninvasive assessments of the structural, biomechanical, and biochemical characteristics of the sclera and cornea. Although important technical challenges remain to the application in vivo, this technique has the potential to enable cross-sectional and longitudinal monitoring of the functional microstructures of the eye and their relationship with aging and diseases involving the corneoscleral shell, such as acute and chronic ocular hypertension, glaucoma, and myopia.

References

1. Maurice DM. *The Cornea and Sclera*. 3rd ed. New York: Academic Press; 1984.

2. Foster CS, de la Maza MS. *The Sclera*. New York: Springer-Verlag; 1994.

3. Yamabayashi S, Ohno S, Aguilar RN, Furuya T, Hosoda M, Tsukahara S. Ultrastructural studies of collagen fibers of the cornea and sclera by a quick-freezing and deep-etching method. *Ophthalmic Res*. 1991;23:320–329.

4. Rada JA, Shelton S, Norton TT. The sclera and myopia. *Exp Eye Res*. 2006;82:185–200.

5. Pijanka JK, Coudrillier B, Ziegler K, et al. Quantitative mapping of collagen fiber orientation in non-glaucoma and glaucoma posterior human sclerae. *Invest Ophthalmol Vis Sci*. 2012;53:5258–5270.

6. Sigal IA, Flanagan JG, Ethier CR. Factors influencing optic nerve head biomechanics. *Invest Ophthalmol Vis Sci*. 2005;46:4189–4199.

7. Quigley HA. Glaucoma: macrocosm to microcosm the Friedenwald lecture. *Invest Ophthalmol Vis Sci*. 2005;46:2662–2670.

8. Chan KC, Fu QL, Hui ES, So KF, Wu EX. Evaluation of the retina and optic nerve in a rat model of chronic glaucoma using in vivo manganese-enhanced magnetic resonance imaging. *Neuroimage*. 2008;40:1166–1174.

9. Chan KC, Fan SJ, Chan RW, Cheng JS, Zhou IY, Wu EX. In vivo visuotopic brain mapping with manganese-enhanced MRI and resting-state functional connectivity MRI. *Neuroimage*. 2014;90:235–245.

10. Shih YY, De la Garza BH, Muir ER, et al. Lamina-specific functional MRI of retinal and choroidal responses to visual stimuli. *Invest Ophthalmol Vis Sci*. 2011;52:5303–5310.

11. Berkowitz BA, Sato Y, Wilson CA, de Juan E. Blood-retinal barrier breakdown investigated by real-time magnetic resonance imaging after gadolinium-diethylenetriaminepentaacetic acid injection. *Invest Ophthalmol Vis Sci*. 1991;32:2854–2860.

12. Chan KC, Cheng JS, Fan S, Zhou IY, Yang J, Wu EX. In vivo evaluation of retinal and callosal projections in early postnatal development and plasticity using manganese-enhanced MRI and diffusion tensor imaging. *Neuroimage*. 2012;59:2274–2283.

13. Cheng H, Nair G, Walker TA, et al. Structural and functional MRI reveals multiple retinal layers. *Proc Natl Acad Sci U S A*. 2006;103:17525–17530.

14. Duong TQ, Ngan SC, Ugurbil K, Kim SG. Functional magnetic resonance imaging of the retina. *Invest Ophthalmol Vis Sci*. 2002;43:1176–1181.

15. Chan KC, Fu QL, Guo H, So KF, Wu EX. GD-DTPA enhanced MRI of ocular transport in a rat model of chronic glaucoma. *Exp Eye Res*. 2008;87:334–341.

16. Berkowitz BA, Roberts R, Luan H, Peysakhov J, Mao X, Thomas KA. Dynamic contrast-enhanced MRI measurements of passive permeability through blood retinal barrier in diabetic rats. *Invest Ophthalmol Vis Sci*. 2004;45:2391–2398.

17. Ho LC, Conner IP, Do CW, et al. In vivo assessment of aqueous humor dynamics upon chronic ocular hypertension and hypotensive drug treatment using gadolinium-enhanced MRI. *Invest Ophthalmol Vis Sci*. 2014;55:3747–3757.

18. Sadun AA, Carelli V, Bose S, Ross-Cisneros FN, Barboni P, Ahrens ET. First application of extremely high-resolution magnetic resonance imaging to study microscopic features of normal and LHON human optic nerve. *Ophthalmology*. 2002;109:1085–1091.

19. Norman RE, Flanagan JG, Rausch SM, et al. Dimensions of the human sclera: thickness measurement and regional changes with axial length. *Exp Eye Res*. 2010;90:277–284.

20. Georgouli T, Chang B, Nelson M, et al. Use of high-resolution microscopy coil MRI for depicting orbital anatomy. *Orbit*. 2008;27:107–114.

21. Goodall N, Kisiswa L, Prashar A, et al. 3-Dimensional modelling of chick embryo eye development and growth using high resolution magnetic resonance imaging. *Exp Eye Res*. 2009;89:511–521.

22. Singh KD, Logan NS, Gilmartin B. Three-dimensional modeling of the human eye based on magnetic resonance imaging. *Invest Ophthalmol Vis Sci*. 2006;47:2272–2279.

23. Langner S, Martin H, Terwee T, et al. 7.1 T MRI to assess the anterior segment of the eye. *Invest Ophthalmol Vis Sci*. 2010;51:6575–6581.

24. Duong TQ, Pardue MT, Thule PM, et al. Layer-specific anatomical, physiological and functional MRI of the retina. *NMR Biomed*. 2008;21:978–996.

25. Nguyen C, Cone FE, Nguyen TD, et al. Studies of scleral biomechanical behavior related to susceptibility for retinal ganglion cell loss in experimental mouse glaucoma. *Invest Ophthalmol Vis Sci*. 2013;54:1767–1780.

26. Sigal IA, Ethier CR. Biomechanics of the optic nerve head. *Exp Eye Res*. 2009;88:799–807.

27. Xia Y. Magic-angle effect in magnetic resonance imaging of articular cartilage: a review. *Invest Radiol*. 2000;35:602–621.

28. Fullerton GD, Cameron IL, Ord VA. Orientation of tendons in the magnetic field and its effect on T2 relaxation times. *Radiology*. 1985;155:433–435.

29. Erickson SJ, Cox IH, Hyde JS, Carrera GF, Strandt JA, Estkowski LD. Effect of tendon orientation on MR imaging signal intensity: a manifestation of the "magic angle" phenomenon. *Radiology*. 1991;181:389–392.

30. Peterfy CG, Janzen DL, Tirman PF, van Dijke CF, Pollack M, Genant HK. "Magic-angle" phenomenon: a cause of increased signal in the normal lateral meniscus on short-TE MR images of the knee. *AJR Am J Roentgenol*. 1994;163:149–154.

31. Werpy NM, Ho CP, Kawcak CE. Magic angle effect in normal collateral ligaments of the distal interphalangeal joint in horses imaged with a high-field magnetic resonance imaging system. *Vet Radiol Ultrasound*. 2010;51:2–10.

32. Erickson SJ, Prost RW, Timins ME. The "magic angle" effect: background physics and clinical relevance. *Radiology*. 1993; 188:23–25.

33. Benjamin M, Bydder GM. Magnetic resonance imaging of entheses using ultrashort TE (UTE) pulse sequences. *J Magn Reson Imaging*. 2007;25:381–389.

34. Rubenstein JD, Kim JK, Morova-Protzner I, Stanchev PL, Henkelman RM. Effects of collagen orientation on MR imaging characteristics of bovine articular cartilage. *Radiology*. 1993; 188:219–226.

35. Henkelman RM, Stanisz GJ, Kim JK, Bronskill MJ. Anisotropy of NMR properties of tissues. *Magn Reson Med*. 1994;32:592–601.

36. Mershon C, Squires A, Gao Y, Chan KC, Tse Z. Magic angle enhanced imaging in high-field MRI using an automated MR-conditional positioner. *Proc Intl Soc Magn Reson Med*. 2013; 21:3474.

37. Mountain KM, Bjarnason TA, Dunn JF, Matyas JR. The functional microstructure of tendon collagen revealed by high-field MRI. *Magn Reson Med*. 2011;66:520–527.

38. Diamant J, Keller A, Baer E, Litt M, Arridge RG. Collagen; ultrastructure and its relation to mechanical properties as a function of ageing. *Proc R Soc Lond B Biol Sci*. 1972;180:293–315.

39. Gathercole LJ, Keller A. Crimp morphology in the fibre-forming collagens. *Matrix*. 1991;11:214–234.

40. Franchi M, Fini M, Quaranta M, et al. Crimp morphology in relaxed and stretched rat Achilles tendon. *J Anat*. 2007;210:1–7.

41. Grytz R, Meschke G. Constitutive modeling of crimped collagen fibrils in soft tissues. *J Mech Behav Biomed Mater*. 2009;2:522–533.

42. Elliott DH. Structure and function of mammalian tendon. *Biol Rev Camb Philos Soc*. 1965;40:392–421.

43. Vidik A, Ekholm R. Light and electron microscopic studies of callagen fibers under strain. *Z Anat Entwicklungsgesch*. 1968; 127:154–164.

44. Rigby BJ, Hirai N, Spikes JD, Eyring H. The mechanical properties of rat tail tendon. *J Gen Physiol*. 1959;43:265–283.

45. Pierre-Jerome C, Moncayo V, Terk MR. MRI of the Achilles tendon: a comprehensive review of the anatomy, biomechanics, and imaging of overuse tendinopathies. *Acta Radiol*. 2010; 51:438–454.

46. Dohlman CH, Bostrom H. Uptake of sulfate by mucopolysaccharides in the rat cornea and sclera. *Acta Ophthalmol*. 1955; 33:455–461.

47. Kaye GI. Stereologic measurement of cell volume fraction of rabbit corneal stroma. *Arch Ophthalmol*. 1969;82:792–794.

48. Winkler M, Shoa G, Xie Y, et al. Three-dimensional distribution of transverse collagen fibers in the anterior human corneal stroma. *Invest Ophthalmol Vis Sci*. 2013;54:7293–7301.

49. Winkler M, Chai D, Kriling S, et al. Nonlinear optical macroscopic assessment of 3-D corneal collagen organization and axial biomechanics. *Invest Ophthalmol Vis Sci*. 2011;52: 8818–8827.

50. William T, Jaeger EA. *Duane's Ophthalmology on DVD-ROM Edition 2006* [DVD]. Philadelphia, PA: Lippincott Williams & Wilkins; 2006;8.

51. DelMonte DW, Kim T. Anatomy and physiology of the cornea. *J Cataract Refract Surg*. 2011;37:588–598.

52. Meek KM, Boote C. The organization of collagen in the corneal stroma. *Exp Eye Res*. 2004;78:503–512.

53. Fullerton GD, Rahal A. Collagen structure: the molecular source of the tendon magic angle effect. *J Magn Reson Imaging*. 2007;25:345–361.

54. McBrien NA, Jobling AI, Gentle A. Biomechanics of the sclera in myopia: extracellular and cellular factors. *Optom Vis Sci*. 2009;86:E23–E30.

55. Meek KM, Boote C. The use of X-ray scattering techniques to quantify the orientation and distribution of collagen in the corneal stroma. *Prog Retin Eye Res*. 2009;28:369–392.

56. Grytz R, Meschke G. A computational remodeling approach to predict the physiological architecture of the collagen fibril network in corneo-scleral shells. *Biomech Model Mechanobiol*. 2010;9:225–235.

57. Fazio MA, Grytz R, Morris JS, et al. Age-related changes in human peripapillary scleral strain. *Biomech Model Mechanobiol*. 2013;13:551–563.

58. Girard MJ, Dahlmann-Noor A, Rayapureddi S, et al. Quantitative mapping of scleral fiber orientation in normal rat eyes. *Invest Ophthalmol Vis Sci*. 2011;52:9684–9693.

59. Sigal IA, Grimm JL, Jan NJ, Reid K, Minckler DS, Brown DJ. Eye-specific IOP-induced displacements and deformations of human lamina cribrosa. *Invest Ophthalmol Vis Sci*. 2014;55: 1–15.

60. Bandettini PA, Wong EC, Jesmanowicz A, Hinks RS, Hyde JS. Spin-echo and gradient-echo EPI of human brain activation using BOLD contrast: a comparative study at 1.5 T. *NMR Biomed*. 1994;7:12–20.

61. Choi S, Cheong Y, Lee HJ, Lee SJ, Jin KH, Park HK. AFM study for morphological and mechanical properties of human scleral surface. *J Nanosci Nanotechnol*. 2011;11:6382–6388.

62. Doughty MJ. Observations on the ultrastructure of equatorial scleral collagen fibrils in sheep eyes. *Vet Ophthalmol*. 2012; 15:71–80.

63. Meek KM, Fullwood NJ. Corneal and scleral collagens—a microscopist's perspective. *Micron*. 2001;32:261–272.

64. Danford FL, Yan D, Dreier RA, Cahir TM, Girkin CA, Vande Geest JP. Differences in the region- and depth-dependent microstructural organization in normal versus glaucomatous human posterior sclerae. *Invest Ophthalmol Vis Sci*. 2013;54: 7922–7932.

65. Burgoyne CF. A biomechanical paradigm for axonal insult within the optic nerve head in aging and glaucoma. *Exp Eye Res*. 2011;93:120–132.

66. Du J, Statum S, Znamirowski R, Bydder GM, Chung CB, Ultrashort TE. T1rho magic angle imaging. *Magn Reson Med*. 2013;69:682–687.

67. Menezes NM, Gray ML, Hartke JR, Burstein D. T2 and T1rho MRI in articular cartilage systems. *Magn Reson Med*. 2004;51: 503–509.

68. Kim DK, Ceckler TL, Hascall VC, Calabro A, Balaban RS. Analysis of water-macromolecule proton magnetization transfer in articular cartilage. *Magn Reson Med*. 1993;29:211–215.

69. Saar G, Zhang B, Ling W, Regatte RR, Navon G, Jerschow A. Assessment of glycosaminoglycan concentration changes in the intervertebral disc via chemical exchange saturation transfer. *NMR Biomed*. 2012;25:255–261.

70. Singh A, Haris M, Cai K, et al. Chemical exchange saturation transfer magnetic resonance imaging of human knee cartilage at 3 T and 7 T. *Magn Reson Med*. 2012;68:588–594.

71. Matyas J, Edwards P, Miniaci A, et al. Ligament tension affects nuclear shape in situ: an in vitro study. *Connect Tissue Res*. 1994;31:45–53.

72. Richdale K, Wassenaar P, Teal Bluestein K, et al. 7 Tesla MR imaging of the human eye in vivo. *J Magn Reson Imaging*. 2009;30:924–932.

73. Graessl A, Muhle M, Schwerter M, et al. Ophthalmic magnetic resonance imaging at 7 T using a 6-channel transceiver radiofrequency coil array in healthy subjects and patients with intraocular masses. *Invest Radiol*. 2014;49:260–270.

74. Zhang Y, Nateras OS, Peng Q, et al. Lamina-specific anatomic magnetic resonance imaging of the human retina. *Invest Ophthalmol Vis Sci*. 2011;52:7232–7237.